J 1 – J 2 square lattice antiferromagnetism in the orbitally quenched insulator MoOPO 4

L. Yang, M. Jeong, P. Babkevich, M. Katukuri, B. Nafradi, E. Shaik, A. Magrez, H. Berger, J. Schefer, E. Ressouche, et al.

J_1-J_2 square lattice antiferromagnetism in the orbitally quenched insulator $MoOPO_4$

L. Yang,[1,2] M. Jeong,[1,*] P. Babkevich,[1] V. M. Katukuri,[3] B. Náfrádi,[2] N. E. Shaik,[1] A. Magrez,[4] H. Berger,[4] J. Schefer,[5] E. Ressouche,[6] M. Kriener,[7] I. Živković,[1] O. V. Yazyev,[3] L. Forró,[2] and H. M. Rønnow[1,7,†]

[1]*Laboratory for Quantum Magnetism, Institute of Physics, Ecole Polytechnique Féderale de Lausanne, CH-1015 Lausanne, Switzerland*
[2]*Laboratory of Physics of Complex Matter, Institute of Physics, Ecole Polytechnique Féderale de Lausanne, CH-1015 Lausanne, Switzerland*
[3]*Chair of Computational Condensed Matter Physics, Institute of Physics, Ecole Polytechnique Féderale de Lausanne, CH-1015 Lausanne, Switzerland*
[4]*Crystal Growth Facility, Institute of Physics, Ecole Polytechnique Féderale de Lausanne, CH-1015 Lausanne, Switzerland*
[5]*Laboratory for Neutron Scattering and Imaging, Paul Scherrer Institute, CH-5232 Villigen, Switzerland*
[6]*Université Grenoble Alpes, CEA, INAC, MEM, F-38000 Grenoble, France*
[7]*RIKEN Center for Emergent Matter Science, Wako, Saitama 351-0198, Japan*

(Received 17 May 2017; published 28 July 2017)

We report magnetic and thermodynamic properties of a $4d^1$ (Mo^{5+}) magnetic insulator $MoOPO_4$ single crystal, which realizes a J_1-J_2 Heisenberg spin-1/2 model on a stacked square lattice. The specific-heat measurements show a magnetic transition at 16 K which is also confirmed by magnetic susceptibility, ESR, and neutron diffraction measurements. Magnetic entropy deduced from the specific heat corresponds to a two-level degree of freedom per Mo^{5+} ion, and the effective moment from the susceptibility corresponds to the spin-only value. Using *ab initio* quantum chemistry calculations, we demonstrate that the Mo^{5+} ion hosts a purely spin-1/2 magnetic moment, indicating negligible effects of spin-orbit interaction. The quenched orbital moments originate from the large displacement of Mo ions inside the MoO_6 octahedra along the apical direction. The ground state is shown by neutron diffraction to support a collinear Néel-type magnetic order, and a spin-flop transition is observed around an applied magnetic field of 3.5 T. The magnetic phase diagram is reproduced by a mean-field calculation assuming a small easy-axis anisotropy in the exchange interactions. Our results suggest 4*d* molybdates as an alternative playground to search for model quantum magnets.

DOI: 10.1103/PhysRevB.96.024445

I. INTRODUCTION

The 4*d* transition-metal oxides naturally bridge the two different regimes of the strongly correlated 3*d* compounds and the 5*d* compounds with strong spin-orbit coupling (SOC) [1]. To what extent the 4*d* compounds represent either regime or display original properties is largely an open question of current interest [2]. Most notably, for instance, it is intriguing that seemingly similar Ca_2RuO_4 and Sr_2RuO_4 display totally different behaviors: the former is a Mott insulator [3–6], while the latter is a metal and becomes superconducting at low temperature [5–8]. Despite great interest, however, purely 4*d* quantum (spin-1/2) magnets are rather rare [9–12] as the electronic structure is often complicated by the presence of other types of 3*d* or 4*f* magnetic orbitals [13].

Among the few known $4d^1$ magnets [9,11,12] the molybdenum phosphate $MoOPO_4$ is reported [14]. The MoO_6 octahedra with Mo^{5+} ions are corner shared to form a chain along the crystallographic *c* axis of the tetragonal structure [Fig. 1(a)], and these chains are further coupled to each other via corner sharing PO_4 tetrahedra [Fig. 1(b)] [14,15]. Previous susceptibility data on a powder sample of $MoOPO_4$ shows a Curie-Weiss behavior with antiferromagnetic $\Theta_{CW} = -14.5$ K and a magnetic transition at 18 K [16]. The ^{31}P NMR on a powder evidences a substantial exchange through the PO_4 tetrahedra, and a sharp powder ESR line infers a rather isotropic *g* factor [16]. However, so far there have not been any studies on the magnetic structure in the ordered state or magnetic properties of a single crystal. Moreover, any discussion on the possible interplay between the crystal electric field and SOC is absent.

Here we report the magnetic and thermodynamic properties of a $MoOPO_4$ single crystal using specific heat, susceptibility, magnetization, ESR, and neutron diffraction experiments. We also elucidate the electronic states and magnetic aspects in light of SOC and crystal-field effects, with the help of *ab initio* quantum-chemistry calculations.

II. EXPERIMENTAL DETAILS

High-quality single crystals of $MoOPO_4$ were grown following the procedure described in Ref. [14]. H_2MoO_4 was mixed with concentrated phosphoric acid and heated up to 1000 °C for reaction in an open platinum crucible. After being cooled to room temperature, the resulting dark-blue solid was dissolved in a large amount of hot water. The yellow transparent crystals were obtained in a platelike shape [Fig. 1(c)]. Large crystals have a typical dimension of $3 \times 2 \times 0.4$ mm^3 with the *c* axis normal to the plate. The crystal belongs to the space group $P4/n$, with lattice parameters of $a = b = 6.2044$ Å and $c = 4.3003$ Å, obtained by single-crystal x-ray diffraction, in agreement with Ref. [14].

Specific heat was measured using a physical properties measurement system (PPMS, Quantum Design, Inc.), and magnetization was measured using a magnetic properties measurement system (MPMS, Quantum Design, Inc.). ESR measurements were performed using a Bruker *X*-band spectrometer with a TE_{102} resonant cavity around 9.4 GHz.

*minki.jeong@gmail.com
†henrik.ronnow@epfl.ch

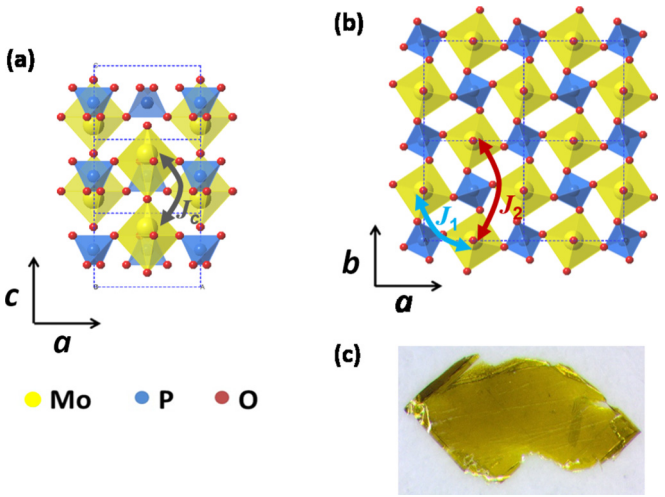

FIG. 1. Crystal structure of $MoOPO_4$ projected onto (a) the ac planes, showing a chainlike arrangement of MoO_6 octahedra (yellow), and (b) the ab planes, showing the coupling between the chains via PO_4 tetrahedra (blue). Dashed lines represent the unit cells. Possible in-plane (J_1 and J_2) and out-of-plane (J_c) exchange couplings are also shown. (c) Photograph of a representative single crystal.

Neutron diffraction experiments were performed on TRICS and D23 beamlines at the Paul Scherrer Institute and Institut Laue-Langevin, respectively. An incident neutron wavelength of 2.3109 Å was employed.

III. RESULTS

A. Specific heat

Figure 2(a) shows the specific heat C_p measured from 2 to 150 K in zero field and in a magnetic field of 14 T. C_p above 25 K for both fields is essentially the same, increasing monotonically with increasing temperature. In zero field a pronounced peak is found at 16.1 K, while the peak is shifted to a slightly lower temperature of 15.4 K at 14 T. These peaks correspond to a transition into a magnetically long range ordered phase, as evidenced by other experimental measurements discussed in later sections.

In order to extract the magnetic part of the specific heat C_{mag} and to deduce the corresponding entropy S_{mag}, we simulate the lattice contribution from the high-temperature data by taking into account the Debye and Einstein contributions. We fit the C_p data above 30 K by a lattice-only model, $C_p = C_D + \sum_i C_{E,i}$, where C_D and $C_{E,i}$ represent the Debye and Einstein terms, respectively. The Debye term is expressed as

$$C_D = 9n_D R\left(\frac{T}{\Theta_D}\right)^3 \int_0^{\Theta_D/T} \frac{x^4 e^x}{(e^x-1)^2} dx, \qquad (1)$$

and the Einstein term is expressed as

$$C_E = 3n_E R \frac{y^2 e^y}{(e^y-1)^2}, \quad y \equiv \Theta_E/T, \qquad (2)$$

where R denotes the gas constant, Θ_D and Θ_E are the Debye and Einstein temperatures, and n_D and n_E are the numbers of

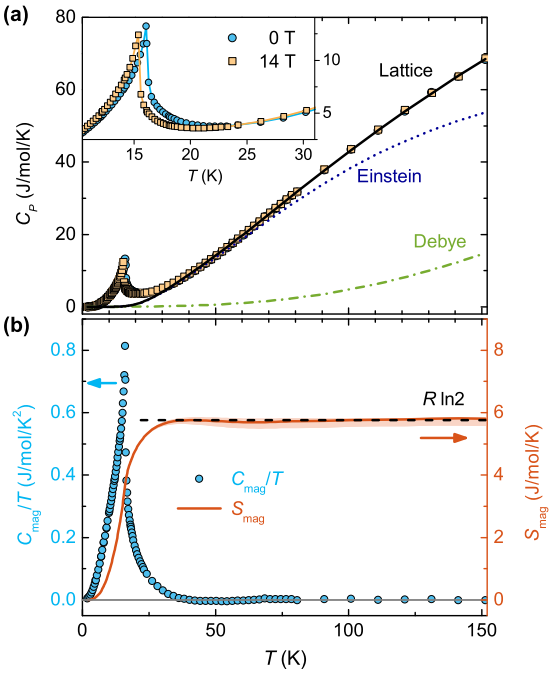

FIG. 2. (a) Specific heat C_p as a function of temperature in zero field (circles) and at 14 T (squares). The solid line represents the best fit of the simulated lattice contribution using the Debye (dash-dotted line) and Einstein (dotted line) terms. The inset provides an enlarged view of the low-temperature region. (b) Left axis: magnetic part of the specific heat C_{mag} divided by temperature (circles). Right axis: the solid line is the entropy calculated from C_{mag}.

the corresponding modes, respectively; the sum $n_D + n_E$ is the total number of atoms per formula unit. For our purpose, we consider that a phenomenological fit using n_D, n_E, Θ_D, and Θ_E as free parameters is sufficient. The best fit for the zero field was obtained when using one Debye and two Einstein terms, which yields the characteristic temperatures $\Theta_D = 1177$ K, $\Theta_{E,1} = 372$ K, and $\Theta_{E,2} = 154$ K and the numbers $n_D = 4$, $n_{E,1} = 2$, and $n_{E,2} = 1$. The solid line in Fig. 2(a) is the best-fit result for the total lattice contribution, while the dash-dotted and dotted lines are the corresponding Debye and Einstein contributions, respectively. While the parameters in the phenomenological phonon fit may not be directly physical, they provide a parametrization of the lattice contribution to the specific heat, which can be substracted to estimate the magnetic specific heat.

Figure 2(b) shows the resulting C_{mag}/T in zero field (circles, left axis) obtained by subtracting the lattice contribution from the measured C_p. The solid line in Fig. 2(b) plots $S_{\mathrm{mag}}(T)$ obtained by integrating C_{mag}/T over temperature (right axis). $S_{\mathrm{mag}}(T)$ is found to reach and stay at $R\ln 2$ at high temperatures, indicating two-level degrees of freedom. The thin colored band in Fig. 2(b) represents the entropy range obtained when fitting the C_p data by varying the lower bound of temperature between 25 and 35 K to confirm the negligible dependence of the result on the chosen fit range. A similar analysis for the 14 T data (not shown) indicates negligible field effects.

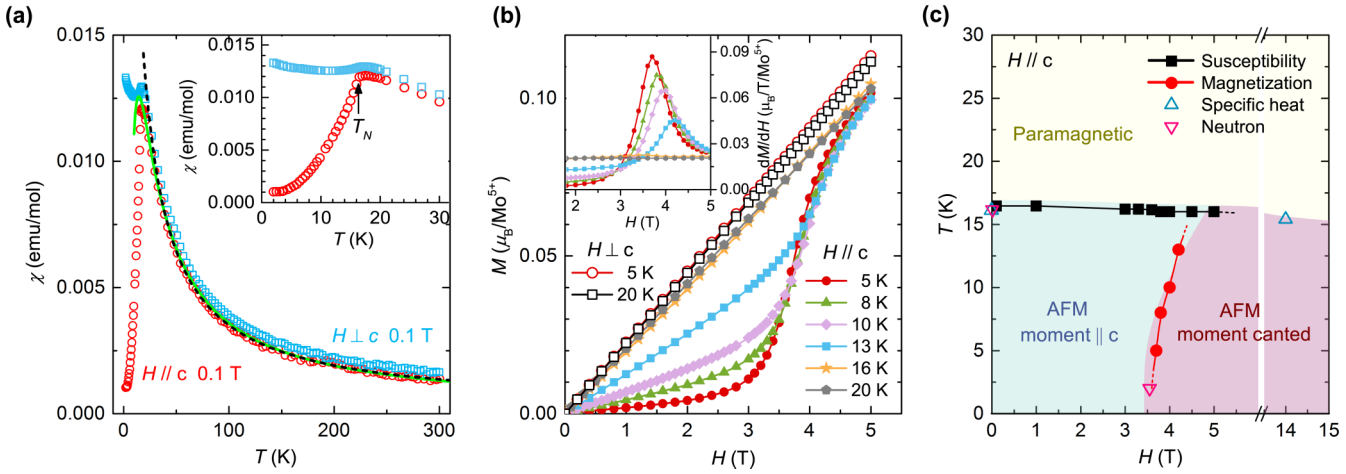

FIG. 3. (a) The dc magnetic susceptibility $\chi(T)$ in a field of $H = 0.1$ T applied parallel (circles) and perpendicular (squares) to the c axis. The dashed line represents the Curie-Weiss fit for $H \parallel c$, and the solid line shows the high-temperature series expansion using the Padé approximant (see the text). The inset shows an enlarged view of the low-temperature region. (b) Isothermal magnetization $M(H)$ for $H \parallel c$ (solid symbols) and $H \perp c$ (open symbols) at several different temperatures. The inset plots the field derivative dM/dH versus H for $H \parallel c$. (c) Magnetic phase diagram from the susceptibility (squares), specific heat (upward triangles), magnetization (circles), and neutron diffraction (downward triangles) data. Lines are guides to the eye. The colored background represents the result from the mean-field calculations (see text).

B. Susceptibility and magnetization

Figure 3(a) shows the dc magnetic susceptibility $\chi = M/H$, where M is magnetization, in a field of $H = 0.1$ T applied parallel and perpendicular to the c axis. For both cases, $\chi(T)$ shows almost identical behavior from 300 down to 20 K. However, for $H \parallel c$, $\chi(T)$ exhibits a sharp drop toward zero as temperature is decreased across 17 K, while the one for $H \perp c$ remains only weakly temperature dependent. This is indicative of an antiferromagnetic transition where the ordered moments at low temperatures are collinear to each other and parallel to the c axis.

The nearly isotropic, high-temperature part of $\chi(T)$ could be well fit by the Curie-Weiss formula, $\chi(T) = C/(T - \Theta_{CW}) + \chi_0$, where Θ_{CW} is the Curie-Weiss temperature and χ_0 is a temperature-independent diamagnetic and background term that may arise from the plastic sample holder or the small amount of grease used. The best and stable fit is obtained in the 50–300 K range, which yields the effective moment $\mu_{\text{eff}} = 1.67(1)\mu_B$ per Mo^{5+} ion, $\Theta_{CW} = -6(1)$ K, and $\chi_0 = 2.2(1) \times 10^{-4}$ emu/mol for $H \parallel c$ and $\mu_{\text{eff}} = 1.69(1)\mu_B$, $\Theta_{CW} = -4(1)$ K, and $\chi_0 = 4.6(1) \times 10^{-4}$ emu/mol for $H \perp c$. The best fit for $H \parallel c$ is shown as a dashed line in Fig. 3(a). The negative Θ_{CW} indicates that antiferromagnetic interactions are dominant. The effective moments indicate a spin-only value consistent with the specific-heat results.

The isothermal magnetization $M(H)$ for $H \parallel c$ and $H \perp c$ at several temperatures is shown in Fig. 3(b). At 5 K, $M(H)$ increases slowly with the field $H \parallel c$ up to 3 T but then sharply increases in a narrow field range of 3–4 T until it eventually converges to the high-temperature $M(H)$ data obtained at 16 or 20 K. This stepwise increase of $M(H)$ becomes smeared out as temperature is increased. On the other hand, no such stepwise behavior was observed at any temperatures for $H \perp c$. These are typical signatures of a spin-flop transition which occurs when the field is applied along an easy axis, along which the ordered moments align: the spins on the two sublattices rotate to attain components perpendicular to the applied field direction as a result of competition between antiferromagnetic coupling, magnetic anisotropy, and the Zeeman energy.

The magnetic phase diagram is thus mapped out by combining the above bulk magnetic and specific-heat results, as shown in Fig. 3(c). The antiferromagnetic transition temperatures in different fields are obtained from the peaks in $\chi(T)$ and $C_p(T)$, and the spin-flop transition fields at different temperatures are obtained from the peak positions in the dM/dH versus H plot [inset of Fig. 3(b)].

C. Electron spin resonance

In order to gain microscopic insight into the magnetic properties, we have performed ESR measurements as a function of field orientation and temperature. Figure 4(a) plots the obtained room-temperature g factor as the field direction is rotated by ϕ in the ab and ac planes. The g factor in the ac plane shows a ϕ variation as large as 2% with characteristic $\cos^2\phi$ angular dependence. On the other hand, the g factor in the ab plane remains essentially constant, as expected from the tetragonal symmetry, within the error of 0.08%, which might have arisen from a slight misorientation of the crystal. We obtain the g factor along the principal axes as $g_a = 1.926(2)$ and $g_c = 1.889(2)$. The average value $g = (2g_a + g_c)/3 = 1.913(2)$ agrees with the one previously obtained by powder ESR [17]. These g values correspond to the effective moments of $1.64\mu_B$ and $1.66\mu_B$ for spin-1/2 for $H \parallel c$ and $H \perp c$, respectively, which are very close to the effective moment values obtained from the Curie-Weiss fit in the previous section.

For a system with tetragonal symmetry with short distances between the transition-metal and ligand ions, one would expect $g_a < g_c$ [18]. However, we find an opposite structure for the g

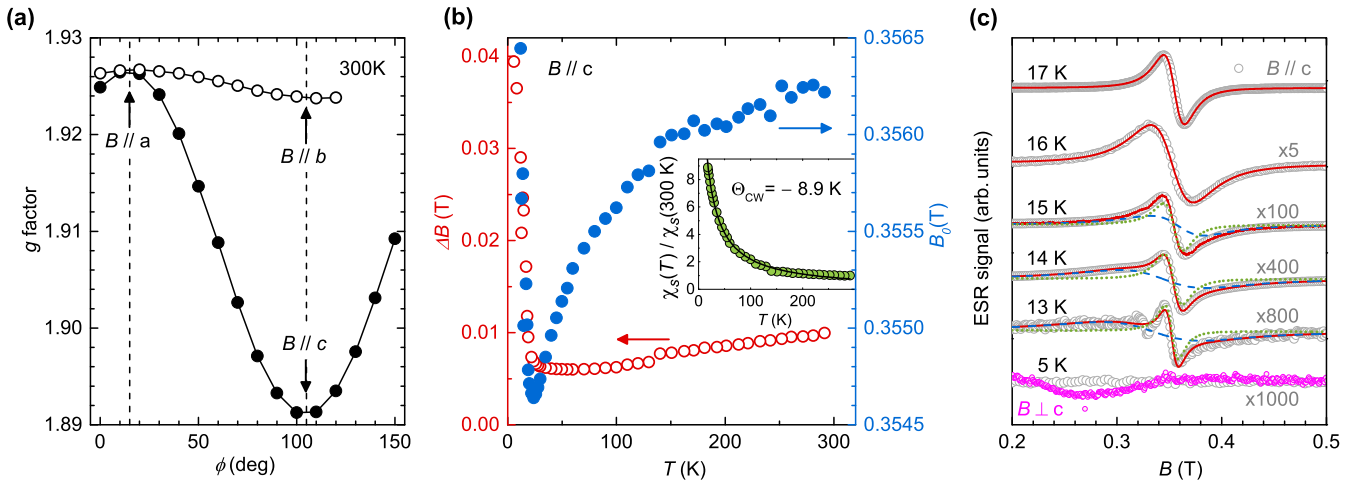

FIG. 4. (a) Angular dependence of the g factor at room temperature from the ESR measurements, where solid symbols are for the field orientation varied on the ac plane and open symbols are for the field orientation varied on the ab plane. (b) Resonance field B_0 (solid circles, right axis) and linewidth ΔB_0 (open circles, left axis) of the ESR spectrum as a function of temperature. The inset plots normalized spin susceptibility $\chi_s(T)/\chi_s(300\,\mathrm{K})$ as a function of temperature. (c) Temperature evolution of the spectrum for $B \parallel c$ across the transition (open circles). The solid line is a sum of two contributions from intrinsic (dotted line) and defect (dashed line) susceptibilities. At 5 K, the data for $B \perp c$ (solid circles) are overlaid.

factor in $MoOPO_4$, even though the orbital energy diagram for the Mo^{5+} ion is expected to be similar to that of tetragonally compressed octahedron with a stabilized d_{xy} orbital (see Fig. 7 below). As explained in Sec. III E, the multiorbital character of the ground state in $MoOPO_4$ results in the observed g values.

Figure 4(b) shows the temperature dependence of the resonance field B_0 and the linewidth ΔB_0 of the ESR spectrum. B_0 slowly decreases as temperature is lowered from 300 down to 24 K, which may be attributed to a lattice contraction. As temperature is further lowered below 24 K, B_0 starts increasing sharply, which indicates that a magnetic transition is approached. Similarly, ΔB_0 slowly decreases as temperature is lowered down to 25 K but then starts broadening significantly as temperature is further lowered down to 15 K due to critical spin fluctuations. The inset of Fig. 4(b) plots the temperature dependence of the local spin susceptibility, which is obtained from the spectral area at each temperature normalized by the one at 300 K, $\chi_s(T)/\chi_s(300\,\mathrm{K})$. The data could be fit to the Curie-Weiss formula with $\Theta_{CW} = -8.9$ K, which is in reasonable agreement with the bulk susceptibility result shown in Fig. 3(a).

Across the transition, the ESR line changes in shape and intensity as shown in Fig. 4(c). The line sustains a perfect Lorentzian shape down to 16 K. On the other hand, the line below 16 K close to the transition fits better to a sum of two Lorentzians: one corresponds to the intrinsic sample susceptibility, while the other may correspond to some defects. Indeed, the ESR signal at the paramagnetic resonance field position below 15 K corresponds to about 0.1% concentration of paramagnetic impurities. The response below 15 K represents the summation of the possible defect contribution and the intrinsic susceptibility. The tiny intrinsic response below the transition temperature may represent clusters of spins that continue to fluctuate within the ESR time window, which essentially disappears at lower temperatures below 14 K. At 5 K, a broad hump of weak signal is observed around 0.27 T for $B \parallel c$ which is absent for $B \perp c$. This signal may correspond to an antiferromagnetic resonance.

D. Neutron diffraction

To determine the microscopic magnetic structure, we have performed neutron diffraction measurements. Magnetic intensity appears at the position of the $k = (100)$ wave vector at 5 K, as shown in the rotation scan in Fig. 5(a). No appreciable change in scattering is found close to (001) between 5 and 25 K, as shown in Fig. 5(b). A small shoulder of the (001) reflection is likely to originate from a closely oriented secondary grain. A nonzero (100) reflection would be consistent with Mo spins

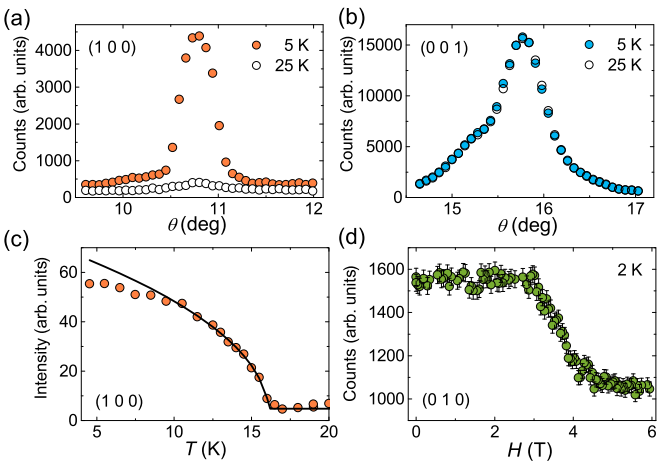

FIG. 5. Neutron diffraction measurements of rotation scans through (a) (100) and (b) (001) reflections recorded at 5 and 25 K. (c) Temperature evolution of the Bragg peak integrated intensity. The solid line is a power-law fit $I(T) \propto (T_N - T)^{2\beta}$ with the parameters $\beta = 0.23$ and $T_N = 16.17 \pm 0.06$ K. (d) The (010) peak counts as a function of magnetic field parallel to the c axis.

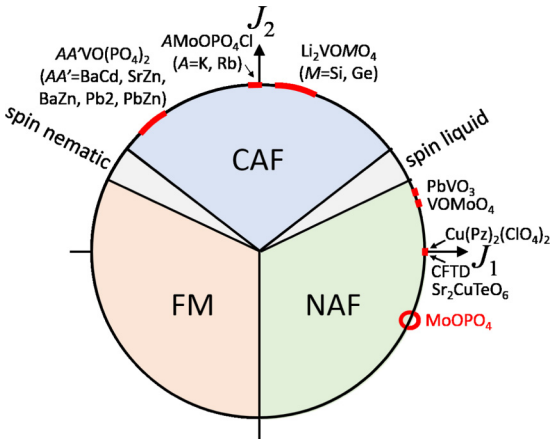

FIG. 6. Schematic phase diagram of the spin-1/2 J_1-J_2 Heisenberg model on a square lattice with corresponding compounds [12]. Different ground states are expected depending on the J_2/J_1 ratio as represented in the diagram, where CAF, NAF, and FM refer to columnar antiferromagnetic, Néel antiferromagnetic, and ferromagnetic ground states, respectively. The present compound, $MoOPO_4$, extends the materials investigation far into the NAF regime.

related by a spatial inversion being antiparallel. Due to the dipolar nature of the magnetic interaction, only magnetization perpendicular to the scattering wave vector gives a nonzero structure factor. As no change is observed for the (001) reflection upon cooling below T_N, we can conclude that the moments are parallel to the c axis. To verify that this is consistent with the symmetry of the lattice and rule out any other magnetic structures, we utilize BASIREPS [19] and outline the results here.

The magnetic representation is decomposed into six one-dimensional irreducible representations Γ_ν whose resulting basis functions are shown in Table I. Examining the results of the irreducible magnetic representations, we find that only Γ_2 is consistent with our observations. These results are in contrast to the closely related AMoO(PO$_4$)Cl (A = K and Rb) materials. Unlike the tilted arrangement of MoO_6 octahedra

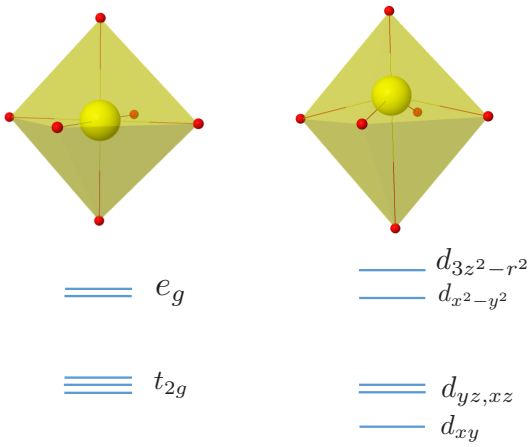

FIG. 7. Single-particle energy-level diagram of d states in an octahedral arrangement of the oxygen ligands (in red) and Mo ion (in yellow) in $MoOPO_4$.

TABLE I. Basis functions of irreducible representation Γ_ν for $k = (100)$ separated into real (Re) and imaginary (Im) components and resolved along the crystallographic axes. The two equivalent Mo_1 and Mo_2 ions are related by an inversion through the origin.

ν		Mo_1	Mo_2
1	Re	(0,0,1)	(0,0,1)
2	Re	(0,0,1)	(0,0,$\bar{1}$)
3	Re	(1,0,0)	(1,0,0)
3	Im	(0,$\bar{1}$,0)	(0,$\bar{1}$,0)
4	Re	(1,0,0)	($\bar{1}$,0,0)
4	Im	(0,$\bar{1}$,0)	(0,1,0)
5	Re	(1,0,0)	(1,0,0)
5	Im	(0,1,0)	(0,1,0)
6	Re	(1,0,0)	($\bar{1}$,0,0)
6	Im	(0,1,0)	(0,$\bar{1}$,0)

and PO_4 tetrahedra in $MoOPO_4$, AMoO(PO$_4$)Cl possesses a higher symmetry where the octahedra and tetrahedra are arranged untilted in the ab plane [20]. Powder neutron diffraction measurements on AMoO(PO$_4$)Cl reveal an antiferromagnetic structure where Mo moments are instead confined to the ab plane [12].

Figure 5(c) shows the temperature dependence of the (100) Bragg peak integrated intensity. By fitting a power-law dependence to the intensity, we find $T_N = 16.17 \pm 0.06$ K, which is consistent with the magnetization and specific-heat measurements. The order parameter exponent is found to be $\beta = 0.23$, corresponding to the two-dimensional XY universality class. However, dedicated measurements with better resolution and separating critical scattering would be needed before any conclusions could be drawn from this. In Fig. 5(d) we show the magnetic Bragg peak intensity as a function of applied field along the c axis recorded at 2 K. Above 3 T, we find a sharp decrease in intensity which then appears to saturate above 5 T. The change in the Bragg peak intensity is consistent with a spin-flop transition that is observed in the magnetization measurements shown in Fig. 3(b). This corresponds to a tilt of the moments by approximately 35° away from the c axis for the fields above 5 T.

E. Model calculations

In order to gain insight into the magnetic interactions, we fit the experimental susceptibility shown in Fig. 3(a) using a high-temperature series expansion [21] assuming a J_1-J_2 spin-1/2 Heisenberg model on a square lattice. The best fit [solid line in Fig. 3(a)] returns $J_1 = 11.4(0.4)$ K and $J_2 = -5.2(1.0)$ K, corresponding to $J_2/J_1 = -0.46$. This ratio supports a collinear Néel order for the ground state (see Fig. 6) in agreement with the neutron diffraction result. Using the mean-field expression for the Curie-Weiss temperature,

$$\Theta_{CW} = -\frac{S(S+1)}{3k_B}\sum_{i=1,2} z_i J_i, \tag{3}$$

where z_i is the number of neighbors for the corresponding couplings (4 for both J_1 and J_2 in the present case), the high-temperature expansion fit yields $\Theta_{CW} = -6.2$ K, which agrees with the value obtained from the simple Curie-Weiss fit. Next,

we simulate the phase diagram using a mean-field calculation. The results are presented by the colored background in Fig. 3(c). A slight exchange anisotropy, $\Delta = 0.02$, has been introduced in the Hamiltonian,

$$\mathcal{H} = J_1 \sum_{\langle i,j \rangle} \left[S_i^x S_j^x + S_i^y S_j^y + (1+\Delta) S_i^z S_j^z \right] + J_2 \sum_{\langle i,k \rangle} \left[S_i^x S_k^x + S_i^y S_k^y + S_i^z S_k^z \right], \quad (4)$$

where $\langle i,j \rangle$ and $\langle i,k \rangle$ refer to the nearest and the next-nearest neighbors in the ab plane, to account for the spin-flop transition in a spin-1/2 system where single-ion anisotropy is not expected to be present. We note that the mean-field calculation reproduces the temperature dependence of the spin-flop field. From the mean-field expression for the Néel temperature,

$$T_N = -\frac{S(S+1)}{3k_B} \sum_{i=1,2} z_i (-1)^i J_i, \quad (5)$$

we obtain $T_N = 16.6(1.4)$ K, which is in excellent agreement with the actual value from the experiments. In the above analyses, we do not include J_c explicitly: although an arbitrarily small J_c is necessary in the actual system to give rise to the (three-dimensional) long-range magnetic ordering, including this parameter in the mean-field calculation produces an insignificant change in the phase diagram. In addition, J_c connects only two neighbors instead of the four of the other couplings in the ab plane, and thus its effect should be correspondingly weaker.

Our methods of analysis do not necessarily select the best model, but rather test the validity and consistency of a proposed one. For instance, ferromagnetic J_c comparable in strength to antiferromagnetic J_1, with negligible J_2, may similarly reproduce our experimental data. However, the ground-state wave function from our *ab initio* quantum-chemistry calculations (see the next section) indicates zero contribution from the out-of-plane orbitals and thus no direct virtual hopping channels for J_c to be appreciable, in contrast to the other coupling on the ab plane.

With strong ferromagnetic second-nearest-neighbor interactions, $MoOPO_4$ populates a region of the J_1-J_2 phase diagram which has so far seen rather few investigations (see Fig. 6). In the context of $(\pi,0)$ zone-boundary anomalies on the square lattice, linear spin-wave theory would for $MoOPO_4$ predict a dispersion with significantly higher energy at $(\pi,0)$ than at $(\pi/2,\pi/2)$, opposite the case of weak antiferromagnetic J_2 in $Cu(pz)_2(ClO_4)_2$ [22]. Compared to the 39% reduction in ordered moment due to quantum fluctuations for the nearest-neighbor Heisenberg model, the estimate for $J_2/J_1 = -0.46$ is only a 24% reduction of the ordered moment. Adding the weak anisotropy for $MoOPO_4$ yields a 21% reduction in ordered moment. Hence quantum fluctuations are likely much weaker in $MoOPO_4$ than in, e.g., $Cu(DCOO)_2 \cdot 4D_2O$, called CFTD for short [23–26] or Sr_2CuTeO_6 [27], and it would be interesting in future investigations to examine whether this leads to a similar suppression of the quantum dispersion and continuum around $(\pi,0)$.

TABLE II. Relative energies of d-level states of the Mo^{5+} ion obtained from CASSCF/NEVPT2 calculations. The corresponding wave functions without (coefficients) and with (weights) SOC at the CASSCF level are also provided, where the up and down arrows signify the S_z values of $+\frac{1}{2}$ and $-\frac{1}{2}$, respectively [41]. At the NEVPT2 level, the wave function would also contain contributions from the inactive and virtual orbitals. For simplicity only the weights of the SOC wave function are provided as the coefficients are complex.

t_{2g}^1 States without SOC	Relative energies (eV)	Wave function (CASSCF) coefficients
$\|\phi_0\rangle$	0	$0.95\,\|xy\rangle - 0.32\,\|x^2-y^2\rangle$
$\|\phi_1\rangle$	1.79	$0.98\,\|yz\rangle + 0.21\,\|zx\rangle$
$\|\phi_2\rangle$	1.79	$0.21\,\|yz\rangle - 0.98\,\|zx\rangle$
$\|\phi_3\rangle$	3.68	$0.32\,\|xy\rangle + 0.95\,\|x^2-y^2\rangle$
$\|\phi_4\rangle$	4.42	$1.00\,\|z^2\rangle$
t_{2g}^1 States with SOC	Relative energy (eV)	Wave function (CASSCF) normalized weights (%)
$\|\psi_0\rangle$	0	$86.0\,\|\phi_0,\uparrow\rangle + 14.0\|\phi_0,\downarrow\rangle$
$\|\psi_1\rangle$	1.75	$50.0\,\|\phi_1,\uparrow\rangle + 50.0\,\|\phi_2,\downarrow\rangle$
$\|\psi_2\rangle$	1.82	$46.0\,\|\phi_1,\uparrow\rangle + 46.0\,\|\phi_2,\uparrow\rangle$ $+4.0\,\|\phi_1,\downarrow\rangle + 4.0\,\|\phi_2,\downarrow\rangle$
$\|\psi_3\rangle$	3.70	$88.0\,\|\phi_3,\uparrow\rangle + 12.0\,\|\phi_3,\downarrow\rangle$
$\|\psi_4\rangle$	4.44	$100.0\,\|\phi_4\rangle$

F. *Ab initio* calculations

An interesting feature in $MoOPO_4$ is that the axial position of the Mo^{4+} ion inside the MoO_6 octahedron is heavily shifted such that the short and long distances to the apical oxygens are 1.652 and 2.641 Å, respectively. As a consequence, the octahedral symmetry around the Mo ion is reduced, resulting in the removal of octahedral orbital degeneracies and an orbitally mixed electronic ground state. To elucidate the electronic levels of the Mo^{5+} ion in low-symmetry crystal fields in $MoOPO_4$, we performed *ab initio* quantum-chemistry calculations using the cluster-in-embedding formalism [28]. A cluster of a single active MoO_6 octahedron along with surrounding nearest-neighbor (NN) PO_4 tetrahedra within the plane and the out-of-plane MoO_6 octahedra embedded in an array of point charges that reproduces the effect of the solid environment [29] was considered for many-body calculations. The NN polyhedra were included within the cluster region to better describe the charge density within the active MoO_6 region. Such calculations have provided excellent insights into the interplay of crystal field and SOC effects for several $4d$ and $5d$ transition-metal compounds [30–33].

A perfect octahedral arrangement of the oxygen ligands around the transition-metal ion splits the d levels into high-energy e_g and low-energy t_{2g} manifolds (see Fig. 7). In $MoOPO_4$, the low-symmetry crystal fields further split the t_{2g} and e_g levels of the Mo^{5+} ion, resulting in an orbital singlet ground state. In Table II the ground-state wave function and the d-d excitations of the Mo^{5+} ion are summarized. These were obtained from many-body multiconfigurational self-consistent field (MCSCF) [34] and N-electron valence-state perturbation theory (NEVPT2) [35] calculations for the atoms in the active cluster region. All-electron Douglas-Kroll-Hess (DKH) basis sets of triple-zeta quality [36] were used to represent the

TABLE III. Computed g factors of $MoOPO_4$ at the NEVPT2 level of theory. The ground-state multiconfiguration wave function as shown in Table II produces the correct structure for the g factors.

CASSCF active orbital space	g_a	g_c
t_{2g}	1.91	1.99
$t_{2g} + e_g$	1.92	1.84

Mo and oxygen ions in the central MoO_6 octahedron, and for the Mo and P ions in the NN polyhedra we employed effective core potentials [37,38] with valence triple-zeta [37] and a single basis function, respectively. The oxygen ions corresponding to the NN MoO_6 and PO_4 polyhedra were expanded in two s and one p atomic natural orbital type [39] functions. All the calculations were performed using the ORCA quantum-chemistry package [40].

In the complete active space formalism of the MCSCF (CASSCF) calculation, a self-consistent wave function was constructed with an active space of one electron in five Mo d orbitals. On top of the CASSCF wave function, NEVPT2 was applied to capture the dynamic electronic correlation. Table II shows that the ground state is predominantly of d_{xy} character but has significant contributions from the $d_{x^2-y^2}$ orbital. The first orbital excitations are nearly degenerate at 1.79 eV and are composed of d_{yz}- and d_{zx}-like orbitals. This scenario is in contrast to the situation in other t_{2g}-active class of compounds with regular transition-metal oxygen octahedra where the t_{2g} manifold remains degenerate with an effective orbital angular momentum $\tilde{l} = 1$. In the latter scenario the spin-orbit interaction admixes all the t_{2g} states to give rise to a total angular momentum J_{eff} ground state [42,43]. Due to the large noncubic crystal-field splittings in the t_{2g} manifold in $MoOPO_4$, the spin-orbit interaction has a negligible effect on the Mo^{5+} ground state ψ_0 (see the with SOC results in Table II). However, the orbital angular momentum is unquenched in d_{zx} and d_{yz}, and hence the SOC results in the splitting of the high-energy states ψ_1 and ψ_2. Our calculations result in excitation energies of 3.68 and 4.42 eV into the e_g states.

To understand the unusual structure of g factors deduced from the ESR experiments, we computed them from the *ab initio* wave function as implemented in ORCA [44]. In Table III, the g factors obtained from CASSCF calculations with two different active orbital spaces, only t_{2g} and $t_{2g} + e_g$, are presented. With only t_{2g} orbitals in the active space, we find $g_a < g_c$ as expected for tetragonal symmetry with the d_{xy}-like orbital occupied in the ground state. By enlarging the active space, the wave function now contains configurations involving the e_g orbitals as well, and this is crucial to produce the experimentally observed g factors with $g_a > g_c$.

IV. CONCLUSION

We have shown with a variety of experimental and computational techniques that $MoOPO_4$ realizes a spin-1/2 magnetic system of $4d^1$ electrons, with the quenched orbital moment due to the large displacement of the Mo ions inside the MoO_6 octahedra. The magnetic ground state supports a Néel-type collinear staggered order on the square lattice with the moments pointing normal to the plane, while the moments align ferromagnetically along the stacking axis. The compound likely realizes a spin-1/2 Heisenberg model on a J_1-J_2 square lattice, with an unfrustrated configuration of antiferromagnetic J_1 and ferromagnetic J_2, while a small interlayer coupling J_c would lead to the observed magnetic ordering transition. The spin-flop transition suggests a small easy-axis anisotropy in the dominant antiferromagnetic exchange, and the mean-field calculation reproduces the experimental magnetic phase diagram. The small anisotropy in the g factor observed in ESR, which is reproduced by the quantum-chemistry calculations, indicates that the ground state involves the higher-energy e_g orbitals in addition to the t_{2g} orbitals. Our results suggest that $4d$ molybdates provide an alternative playground to search for model quantum magnets other than $3d$ compounds.

ACKNOWLEDGMENTS

We thank R. Scopelliti and O. Zaharko for their help with x-ray and neutron diffraction, respectively. We also thank V. Favre and P. Huang for their help with the specific-heat analysis. V.M.K. is grateful to H. Stoll for discussions on effective core potentials. This work was supported by the Swiss National Science Foundation, the MPBH network, and European Research Council grants CONQUEST and TopoMat (No. 306504). M.J. is grateful for support from the European Commission through the Marie Skłodowska-Curie Action COFUND (EPFL Fellows). M.K. is supported by a Grant-in-Aid for Scientific Research (C) (JSPS, KAKENHI No. 15K05140). The *ab initio* calculations were performed at the Swiss National Supercomputing Centre (CSCS) under project s675.

[1] D. Khomskii, *Transition Metal Compounds* (Cambridge University Press, Cambridge, 2014).
[2] W. Witczak-Krempa, G. Chen, Y. B. Kim, and L. Balents, Annu. Rev. Condens. Matter Phys. **5**, 57 (2014).
[3] S. Nakatsuji, S.-i. Ikeda, and Y. Maeno, J. Phys. Soc. Jpn. **66**, 1868 (1997).
[4] G. Cao, S. McCall, M. Shepard, J. E. Crow, and R. P. Guertin, Phys. Rev. B **56**, R2916(R) (1997).
[5] S. Nakatsuji and Y. Maeno, Phys. Rev. Lett. **84**, 2666 (2000).
[6] C. G. Fatuzzo, M. Dantz, S. Fatale, P. Olalde-Velasco, N. E. Shaik, B. D. Piazza, S. Toth, J. Pelliciari, R. Fittipaldi, A. Vecchione, N. Kikugawa, J. S. Brooks, H. M. Rønnow, M. Grioni, Ch. Rüegg, T. Schmitt, and J. Chang, Phys. Rev. B **91**, 155104 (2015).
[7] Y. Maeno, H. Hashimoto, K. Yoshida, S. Nishizaki, T. Fujita, J. Bednorz, and F. Lichtenberg, Nature (London) **372**, 532 (1994).
[8] K. Ishida, H. Mukuda, Y. Kitaoka, K. Asayama, Z. Mao, Y. Mori, and Y. Maeno, Nature (London) **396**, 658 (1998).
[9] M. A. de Vries, A. C. Mclaughlin, and J.-W. G. Bos, Phys. Rev. Lett. **104**, 177202 (2010).
[10] T. Aharen, J. E. Greedan, C. A. Bridges, A. A. Aczel, J. Rodriguez, G. MacDougall, G. M. Luke, T. Imai, V. K.

Michaelis, S. Kroeker, H. Zhou, C. R. Wiebe, and L. M. D. Cranswick, Phys. Rev. B **81**, 224409 (2010).
[11] L. Clark, G. J. Nilsen, E. Kermarrec, G. Ehlers, K. S. Knight, A. Harrison, J. P. Attfield, and B. D. Gaulin, Phys. Rev. Lett. **113**, 117201 (2014).
[12] H. Ishikawa, N. Nakamura, M. Yoshida, M. Takigawa, P. Babkevich, N. Qureshi, H. M. Rønnow, T. Yajima, and Z. Hiroi, Phys. Rev. B **95**, 064408 (2017).
[13] J. S. Gardner, M. J. P. Gingras, and J. E. Greedan, Rev. Mod. Phys. **82**, 53 (2010).
[14] P. Kierkegaard and J. M. Longo, Acta Chem. Scand. **24**, 427 (1970).
[15] E. Canadell, J. Provost, A. Guesdon, M. Borel, and A. Leclaire, Chem. Mater. **9**, 68 (1997).
[16] L. Lezama, K. Suh, G. Villeneuve, and T. Rojo, Solid State Commun. **76**, 449 (1990).
[17] L. Lezama, G. Villeneuve, M. Marcos, J. Pizarro, P. Hagenmuller, and T. Rojo, Solid State Commun. **70**, 899 (1989).
[18] A. Abragam and B. Bleaney, *Electron Paramagnetic Resonance of Transition Ions* (Clarendon, Oxford, 1970).
[19] J. Rodríguez-Carvajal, Phys. B (Amsterdam, Neth.) **192**, 55 (1993).
[20] M. Borel, A. Leclaire, J. Chardon, J. Provost, and B. Raveau, J. Solid State Chem. **137**, 214 (1998).
[21] H.-J. Schmidt, A. Lohmann, and J. Richter, Phys. Rev. B **84**, 104443 (2011).
[22] N. Tsyrulin, F. Xiao, A. Schneidewind, P. Link, H. M. Rønnow, J. Gavilano, C. P. Landee, M. M. Turnbull, and M. Kenzelmann, Phys. Rev. B **81**, 134409 (2010).
[23] H. M. Rønnow, D. F. McMorrow, and A. Harrison, Phys. Rev. Lett. **82**, 3152 (1999).
[24] H. M. Rønnow, D. F. McMorrow, R. Coldea, A. Harrison, I. D. Youngson, T. G. Perring, G. Aeppli, O. Syljuåsen, K. Lefmann, and C. Rischel, Phys. Rev. Lett. **87**, 037202 (2001).
[25] N. B. Christensen, H. M. Rønnow, D. F. McMorrow, A. Harrison, T. Perring, M. Enderle, R. Coldea, L. Regnault, and G. Aeppli, Proc. Natl. Acad. Sci. USA **104**, 15264 (2007).
[26] B. Dalla Piazza, M. Mourigal, N. B. Christensen, G. Nilsen, P. Tregenna-Piggott, T. Perring, M. Enderle, D. F. McMorrow, D. Ivanov, and H. M. Rønnow, Nat. Phys. **11**, 62 (2015).
[27] P. Babkevich, V. M. Katukuri, B. Fåk, S. Rols, T. Fennell, D. Pajić, H. Tanaka, T. Pardini, R. R. P. Singh, A. Mitrushchenkov, O. V. Yazyev, and H. M. Rønnow, Phys. Rev. Lett. **117**, 237203 (2016).
[28] L. Hozoi and P. Fulde, in *Computational Methods for Large Systems*, edited by J. R. Reimers (Wiley, Hoboken, NJ, 2011), pp. 201–224.
[29] M. Klintenberg, S. Derenzo, and M. Weber, Comput. Phys. Commun. **131**, 120 (2000).
[30] V. M. Katukuri, K. Roszeitis, V. Yushankhai, A. Mitrushchenkov, H. Stoll, M. van Veenendaal, P. Fulde, J. van den Brink, and L. Hozoi, Inorg. Chem. **53**, 4833 (2014).
[31] V. M. Katukuri, H. Stoll, J. van den Brink, and L. Hozoi, Phys. Rev. B **85**, 220402(R) (2012).
[32] N. A. Bogdanov, V. M. Katukuri, H. Stoll, J. van den Brink, and L. Hozoi, Phys. Rev. B **85**, 235147 (2012).
[33] X. Liu, V. M. Katukuri, L. Hozoi, W.-G. Yin, M. P. M. Dean, M. H. Upton, J. Kim, D. Casa, A. Said, T. Gog, T. F. Qi, G. Cao, A. M. Tsvelik, J. van den Brink, and J. P. Hill, Phys. Rev. Lett. **109**, 157401 (2012).
[34] T. Helgaker, P. Jørgensen, and J. Olsen, *Molecular Electronic-Structure Theory* (Wiley, Chichester, UK, 2000).
[35] C. Angeli, R. Cimiraglia, and J.-P. Malrieu, Chem. Phys. Lett. **350**, 297 (2001).
[36] D. A. Pantazis, X.-Y. Chen, C. R. Landis, and F. Neese, J. Chem. Theory Comput. **4**, 908 (2008).
[37] K. A. Peterson, D. Figgen, M. Dolg, and H. Stoll, J. Chem. Phys. **126**, 124101 (2007).
[38] G. Igel-Mann, H. Stoll, and H. Preuss, Mol. Phys. **65**, 1321 (1988).
[39] K. Pierloot, B. Dumez, P.-O. Widmark, and B. Roos, Theor. Chim. Acta **90**, 87 (1995).
[40] F. Neese, WIREs Comput. Mol. Sci. **2**, 73 (2012).
[41] The spin-orbit coupling results in an admixture of the t_{2g} states with different S_z; see Ref. [18].
[42] B. J. Kim, H. Ohsumi, T. Komesu, S. Sakai, T. Morita, H. Takagi, and T. Arima, Science **323**, 1329 (2009).
[43] B. J. Kim, H. Jin, S. J. Moon, J.-Y. Kim, B.-G. Park, C. S. Leem, J. Yu, T. W. Noh, C. Kim, S.-J. Oh, J.-H. Park, V. Durairaj, G. Cao, and E. Rotenberg, Phys. Rev. Lett. **101**, 076402 (2008).
[44] F. Neese, Mol. Phys. **105**, 2507 (2007).